Journal of Applied Physics

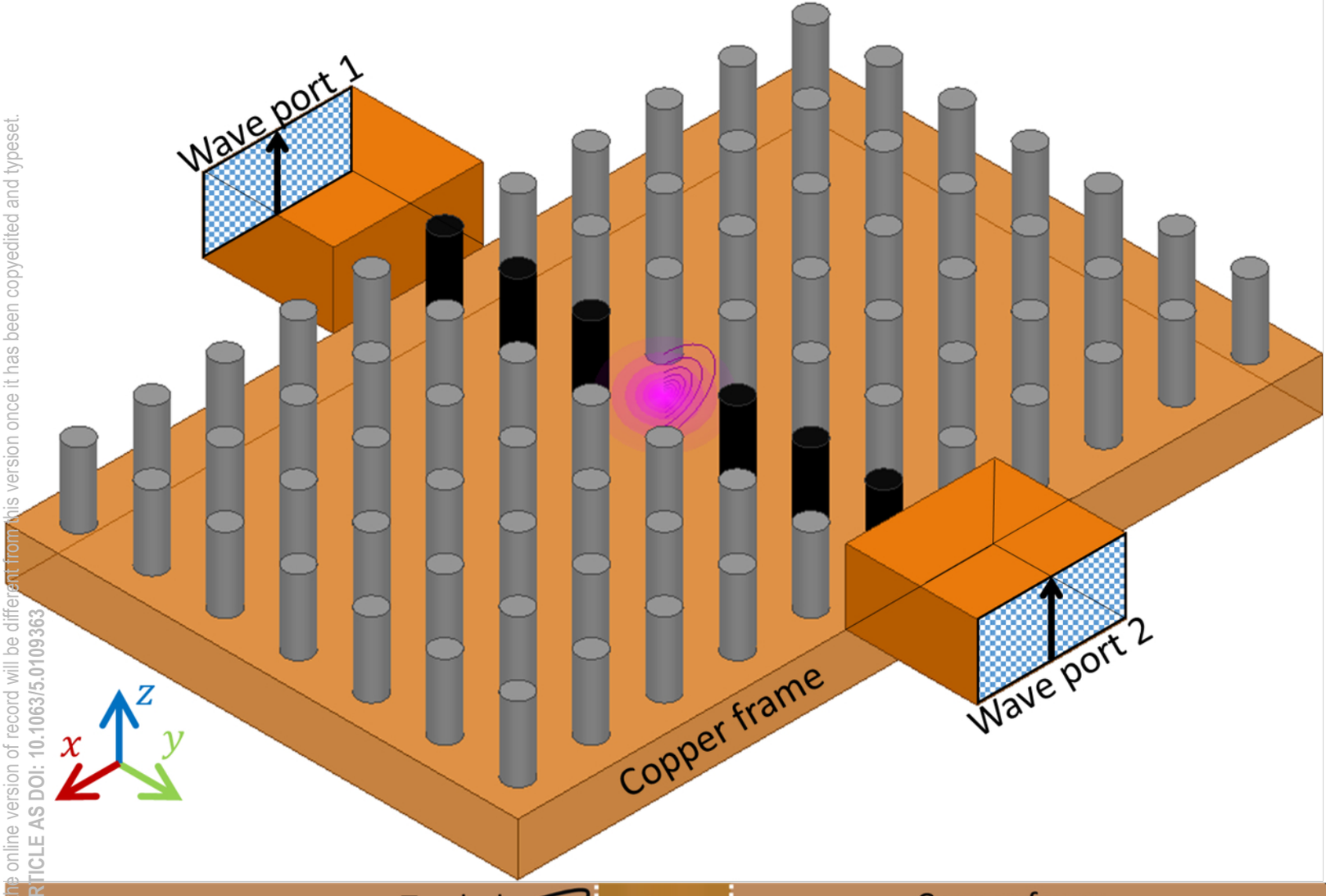

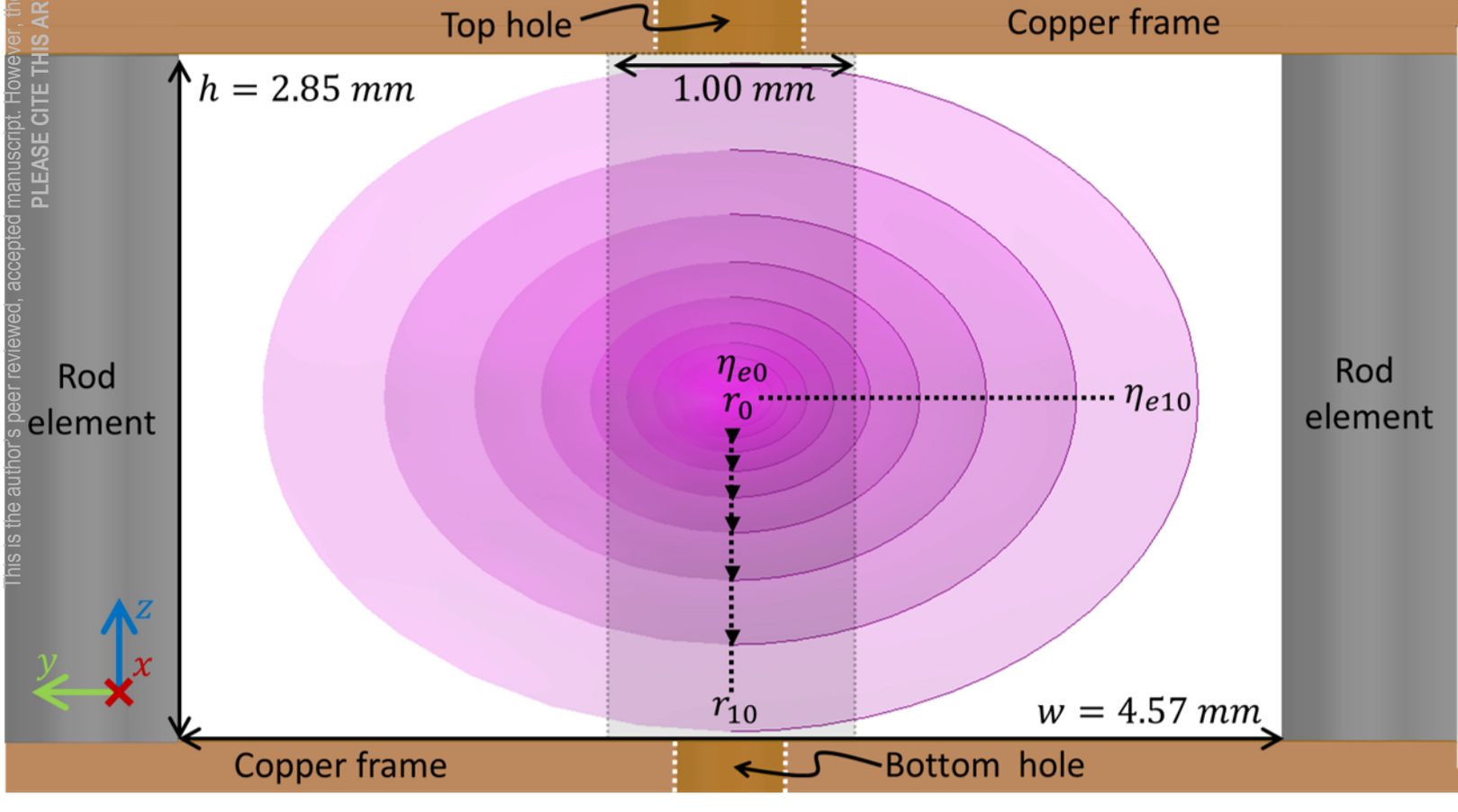

AIP Publishing

Journal of Applied Physics

ACCEPTED MANUSCRIPT

PLEASE CITE THIS ARTICLE AS DOI: 10.1063/5.0109363

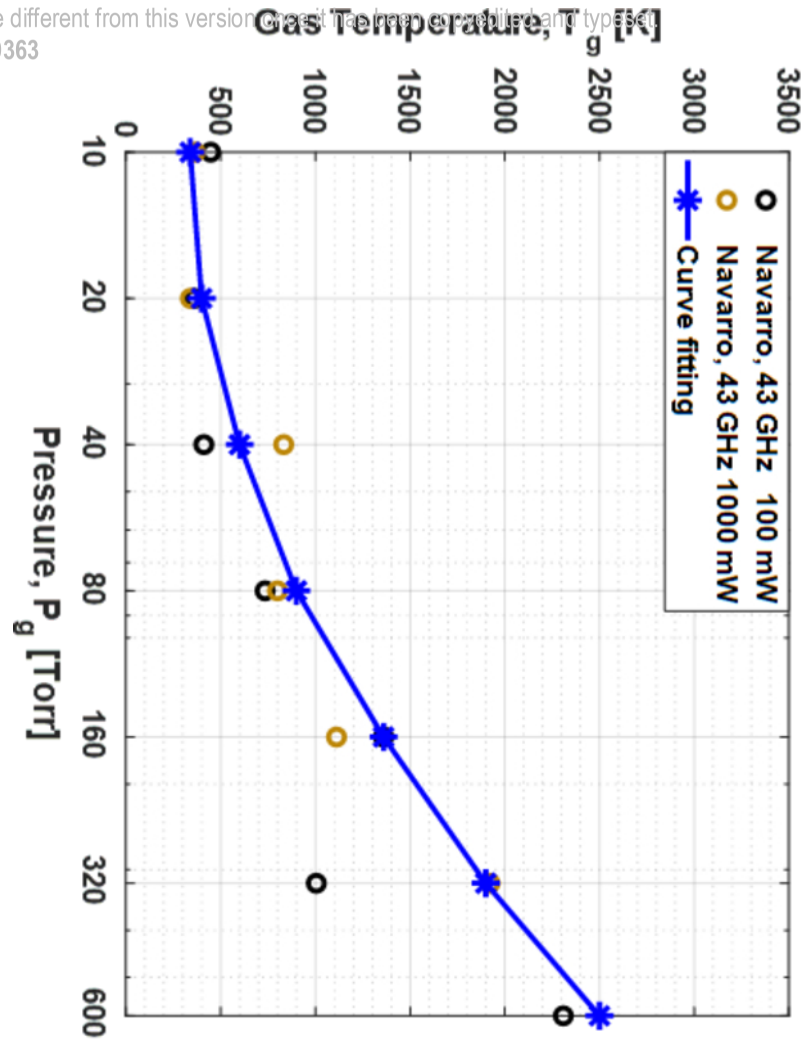

AIP Publishing

Journal of Applied Physics

ACCEPTED MANUSCRIPT

PLEASE CITE THIS ARTICLE AS DOI: 10.1063/5.0109363

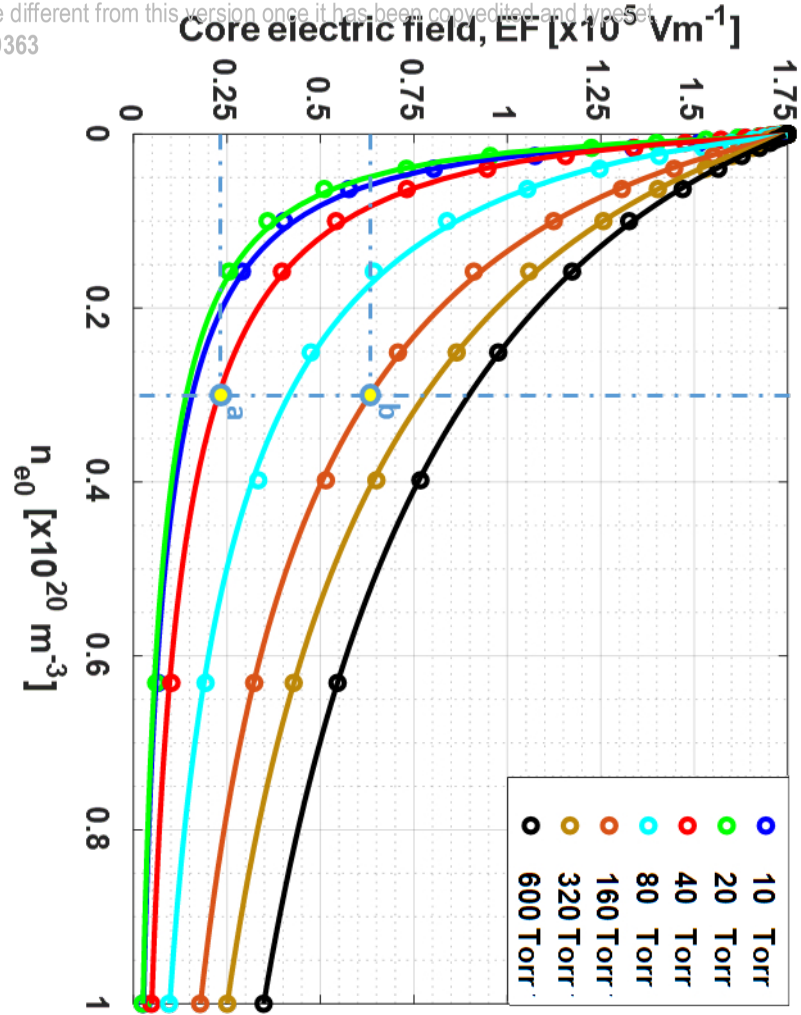

AIP Publishing

Journal of Applied Physics

PLEASE CITE THIS ARTICLE AS DOI: 10.1063/5.0109363

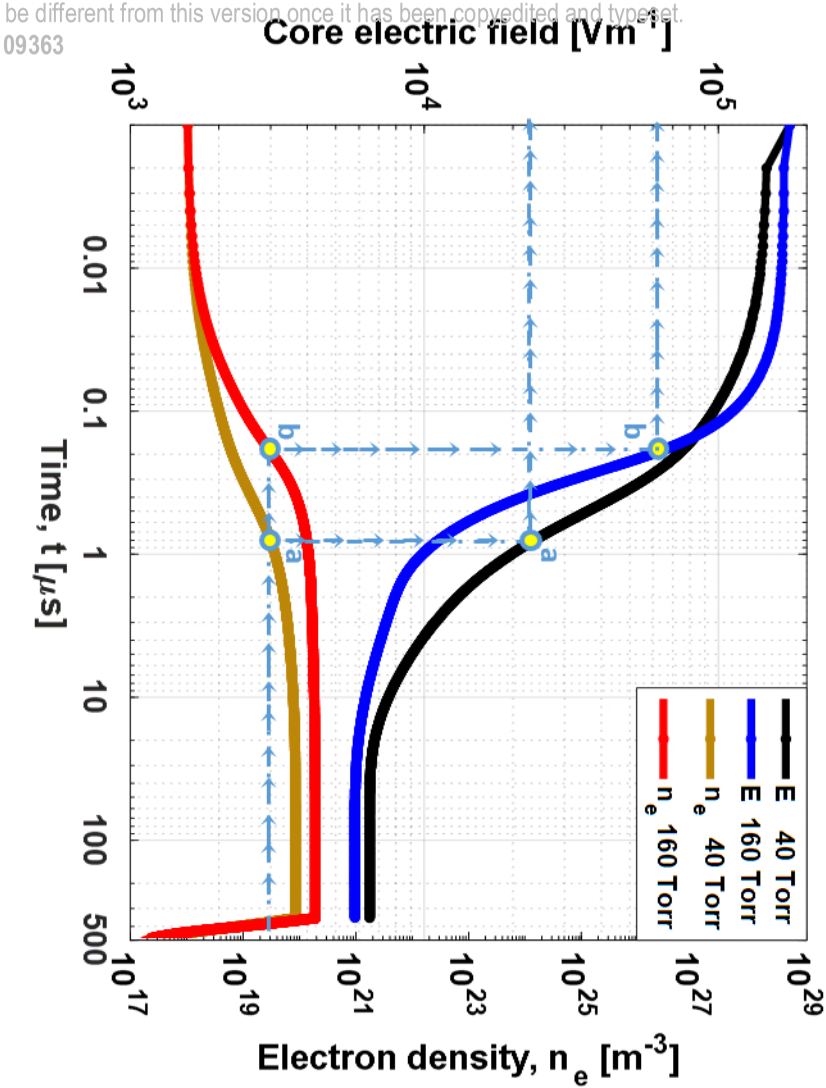

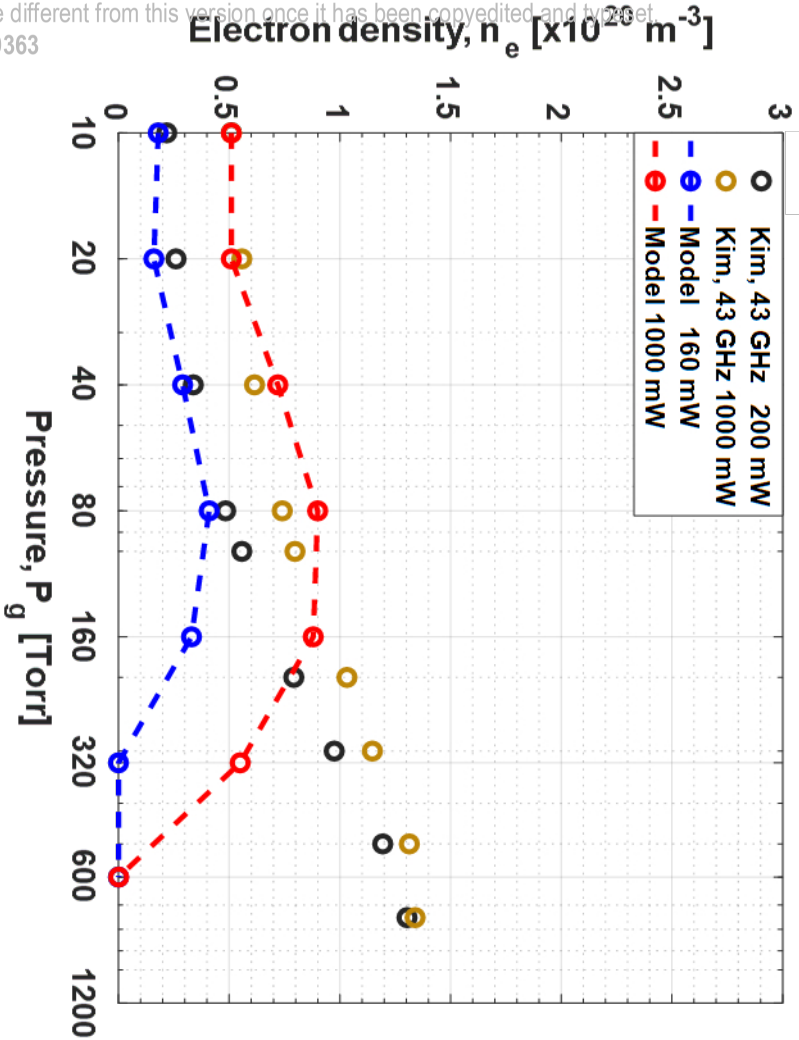

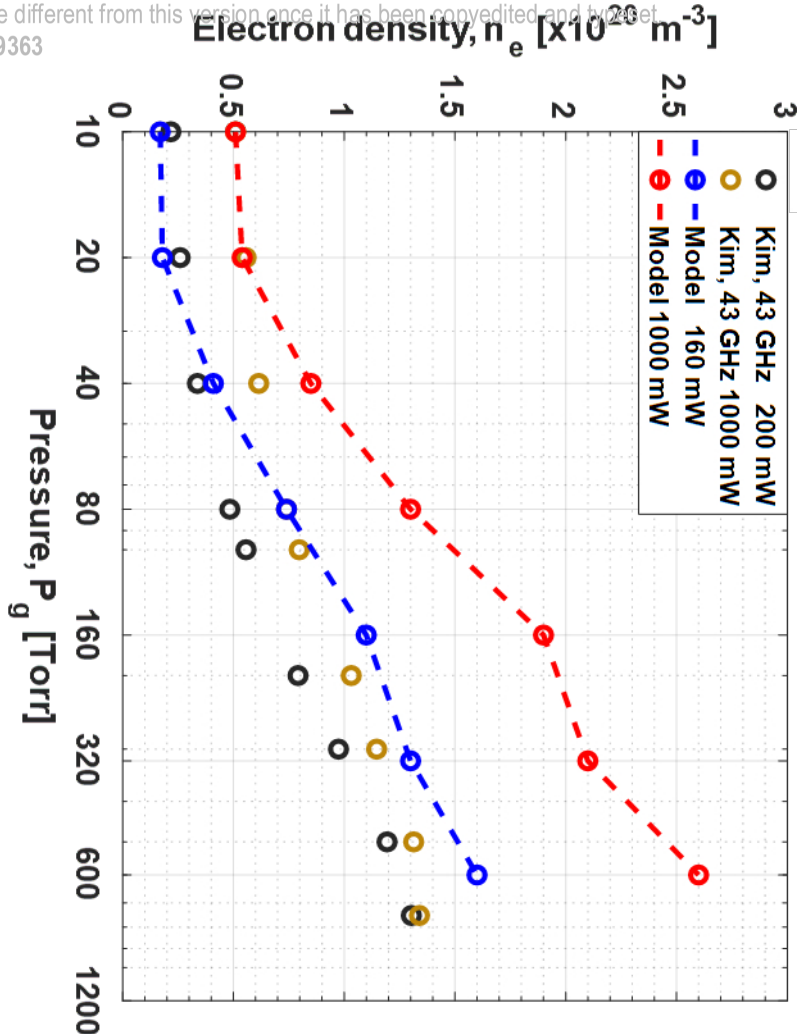

AIP Publishing

Journal of Applied Physics

PLEASE CITE THIS ARTICLE AS DOI: 10.1063/5.0109363

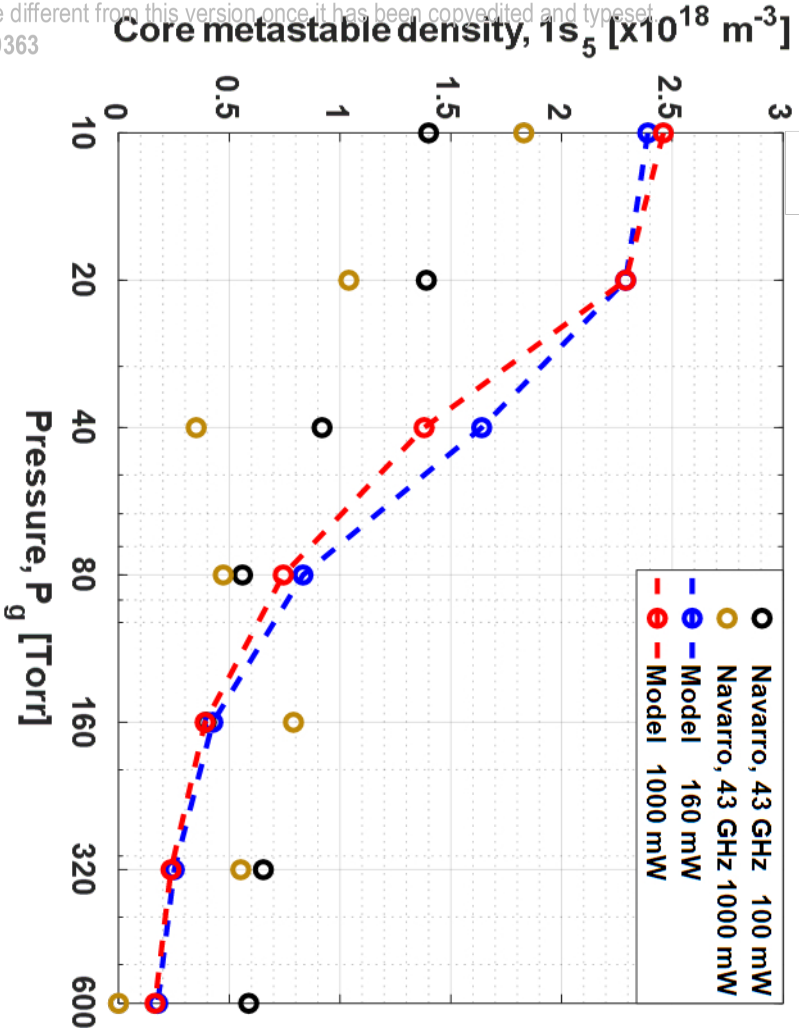

AIP Publishing

Journal of Applied Physics

ACCEPTED MANUSCRIPT

PLEASE CITE THIS ARTICLE AS DOI: 10.1063/5.0109363

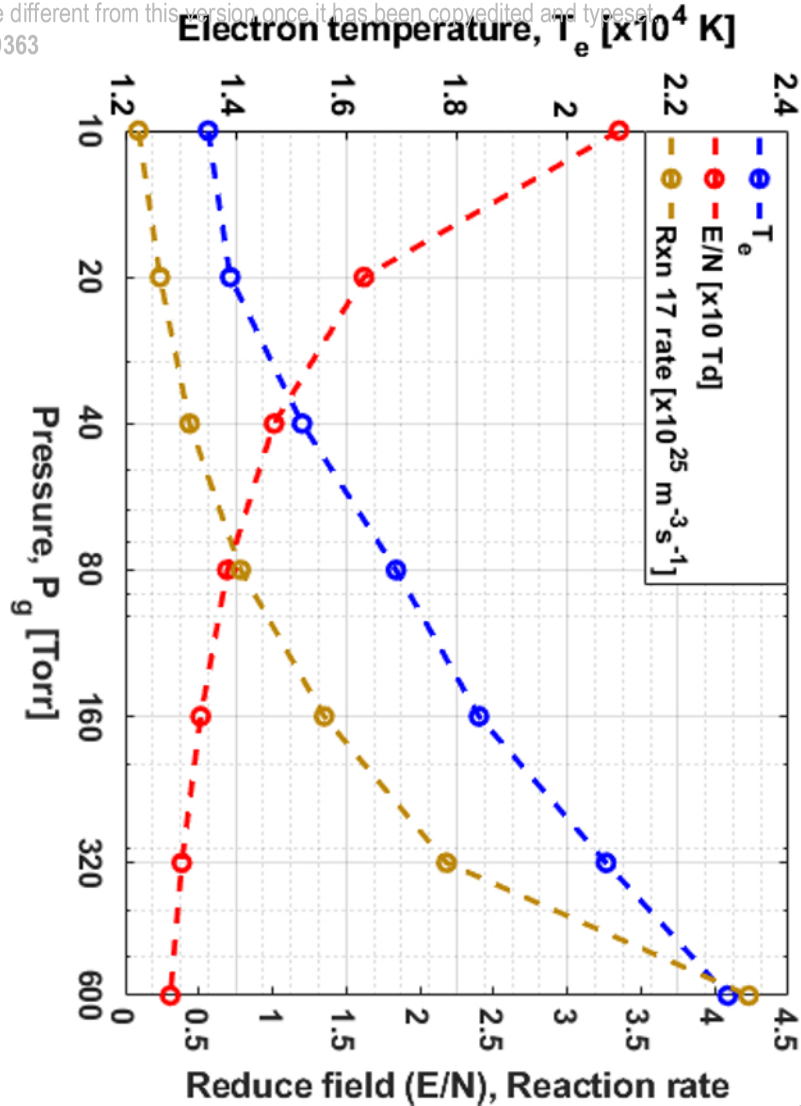

Journal of Applied Physics

Modeling of a 43 GHz Microplasma within a Photonic Crystal

Rafael Navarro and Jeffrey A. Hopwood

Electrical and Computer Engineering Department, Tufts University, Medford, 02155, Massachusetts, USA

E-mail: hopwood@ece.tufts.edu

Received xxxxxx
Accepted for publication xxxxxx
Published xxxxxx

Abstract

The electron density (n_e) and argon metastable density ($1s_5$) of a 43 GHz microplasma are obtained using the Zero-Dimensional Plasma Kinetics solver (ZDPlasKin®) for an incident power of 160 mW and 1000 mW and argon pressures of 10 to 600 Torr ($1.3x10^3$ to $8.0x10^4$ Pa). These simulations are compared with previously published experimental data. To determine the self-consistent electric field in the modeled plasma, the three-dimensional millimeter wave fields are computed as a function of electron density using ANSYS EM19.2, HFSS®. This electromagnetic field model is coupled to ZDPlasKin such that any increase in the simulated plasma density correctly attenuates the simulated electric field within the microplasma. The electron density is found to be sensitive to argon gas temperature, so a two-zone temperature model was needed to obtain agreement with experimental measurements. The temperature in the central core of the microplasma was determined by a previous experimental study. That temperature was used as input to the model for the simulation of volume recombination losses. The outer regions of the microplasma are assumed to be in equilibrium with the walls (300 K). This second temperature was used in the model to determine diffusion losses. The modeled electron and metastable density are the order of 10^{20} m^{-3} and 10^{18} m^{-3} respectively. This is in a good agreement with those measured experimentally as long as the two-zone temperature model is used. In the absence of a hot gas core, the modeled three-body recombination rates are excessive and the simulation severely under-predicts the electron density and over-estimates the metastable density. We conclude that the millimeter wave microplasma has a hot core (2500 K at 600 Torr) that rarifies the argon gas and effectively reduces three-body recombination. This allows one to achieve high electron density on the order of 10^{20} m^{-3} with only 100 mW of wave power.

1. Introduction

Microplasmas are sustained throughout much of the frequency spectrum including DC [1], AC [2], [3], RF [4], [5], as well as the microwave [6], [7] and millimeter wave bands [8]. For instance, in the AC domain plasmas can be ignited by using a dielectric barrier discharge (DBD) [2], [3] in order to operate as sources for emission spectrometry. In the microwave domain, microplasmas have been created using structures such as split ring resonators (SRR's) [9]–[11] and photonic crystals (PhC's) [12], [13]. Beyond the microwave spectrum, there is interest in understanding the behavior of plasma interactions in the millimeter wave [14] and in the THz bands [15]. As the frequency increases, however, one approaches the "THz gap" (0.1 to 10 THz), where power sources are technically challenging and electromagnetic losses begin to dominate in the materials used to form the microplasma sources. This causes the generation and study of electromagnetic interactions with microplasmas to be challenging at extreme frequencies.

To experimentally observe microplasma approaching the terahertz range, photonic crystals have been used to create an electrodeless plasma in the millimeter wave (MMW) band at 43 GHz [16] and 94 GHz [17]. Because a PhC is readily scaled into the optical band, this method offers a technical path toward THz plasma generation.

Journal of Applied Physics

Several microplasma models have been published [18]–[20] in the low THz range (up to 400 GHz). These models only agree for the frequencies below 10 GHz where benchmarking data are available. Unfortunately, the models diverge for higher frequencies. Hence there is a need to have experimental benchmarking data for high frequency operation. Recently, spectroscopic diagnostics [21], [22] have been used to determine some basic parameters of the plasma at 43 GHz. Among these parameters are the electron density n_e, the argon metastable density of the $1s_5$ excited state, and the gas temperature. These new data will be used to guide and validate the model presented in this work.

This paper develops a self-consistent model for the MMW microplasma. The model results are validated using experimental data for the electron and metastable argon density of a microplasma at 43 GHz [21], [22]. This paper is organized as follows: In Sec. II, the microplasma kinetic model is described. A separate electromagnetic model calculates the electric field in three dimensions using the Drude model derived from the plasma solution. This field is iteratively coupled to the plasma model for self-consistency. In Sec. III, the results are presented, including a comparison of the argon metastable density and the electron density between the model and experiment. These results are interpreted in Sec. IV

2. Plasma model

In order to better understand the behavior of the MMW-excited microplasma, a zero-dimensional plasma model has been created and solved using the ZDPlasKin software [23], a plasma kinetics solver developed at the Laboratoire des Plasmas et Conversion d'Energie. Using the BOLSIG+ solver [24], the Boltzmann equation can be solved to calculate the electron energy distribution function (EEDF), and in turn to determine the rate constants for all specified plasma reactions in the model. The plasma model, however, requires an external calculation of the MMW electric field that must be consistent with the modeled electron density. This self-consistent EM model is described later in the section.

2.1 Plasma model description

The input to the plasma model includes gas type (argon), the electromagnetic wave frequency (f in Hz), the electric field (E in $\mathrm{Vm^{-1}}$), gas pressure (P_g in Torr) and temperature (T_g in K). These are used to calculate the gas density (N_g in $\mathrm{m^{-3}}$), the reduced electric field (E/N_g in Td), and the reduced frequency (ω/N_g in $\mathrm{rad.\,m^3.\,s^{-1}}$). Specifying the size of the plasma, which is limited by the copper frame as shown at the bottom of Fig. 1, allows for diffusion losses at the boundary walls.

Included charged species are electrons e, the atomic ion Ar^+, and the molecular ion $Ar_2{}^+$. Considering that metastable density $1s_5$ is the most predominant within the $1s$ level [25], and for simplicity purposes, the different excited neutral states of argon are lumped into effective $1s$ and $2p$ states. Also, one effective excited level of the neutral argon dimer $Ar_2{}^*$, is included. The argon metastable state density is sensitive to impurities, so OH molecular fragments are included. These represent the most common vacuum system impurities from outgassing of water vapor. A density $OH_g = 3.2x10^{20}\ \mathrm{m^{-3}}$ is considered, by assuming a base vacuum pressure of 10^{-2} Torr after evacuation [22].

The plasma model considers 25 reactions, among which are electron-collisions, 3-body recombination, radiative transition and quenching from outgassing species. These reactions are presented in Table I with their reaction rate constants. Some of these rates constants are dependent on T_e, T_g and T_{vib} (vibrational temperature), considering this latter for the Ar_2 species. For instance, in reaction 11, T_{vib} is assumed to be close to T_g [26], which is true in our case where vibrational temperatures in the experiment (obtained from the LIFBASE curve fit) ranges from 2700 to 3200 K [21]. Therefore, T_{vib} will be estimated using T_g in the model. Using BOLSIG+®, the rate constants for electron-driven reactions are calculated through the cross section data from the IST-Lisbon database [27], [28] via the LXCat [29]–[31].

In the model, the losses of the charged species from the plasma are considered by using the diffusion loss rates. These losses are due to the ambipolar diffusion, and the rate constant is estimated by considering the plasma as a rectangular box (L×W×H) with cosine density profiles along the x, y and z axes. Then, the diffusion rate is calculated from $\nu_{diff} = D_a/\Lambda$, where Λ is the effective diffusion length (in $\mathrm{m^2}$) given by:

$$\Lambda = \left(\frac{\pi^2}{L^2} + \frac{\pi^2}{W^2} + \frac{\pi^2}{H^2}\right)^{-1} \qquad (1)$$

However, in the photonic crystal plasma, the plasma is unbounded in the x- and y- directions. So, the most important surface loss is to be found on the z axis as shown in Fig. 1, hence we only considered $H = 2.8\ \mathrm{mm}$. The diffusion coefficient is $D_a = \mu_i(k_B T_e/e)$, in $\mathrm{m^2 s^{-1}}$, where μ_i and T_e are the ion mobility (in $\mathrm{m^2 V^{-1} s^{-1}}$) and the electron temperature (in K), respectively. For Ar^+ in atmospheric pressure and standard temperature (273 K), the mobility is found to be $1.5x10^{-4}\ \mathrm{m^2 V^{-1} s^{-1}}$ [32], [33]. This value is scaled for all pressures in this work as follows [32], [34]:

$$\mu_i = \mu_o \frac{760\ \mathrm{Torr}}{P_g} \frac{T_g}{273\ \mathrm{K}} \qquad (2)$$

Table I. Reactions for the plasma model.

#	Reaction	Rate Constant	Units	Reference
1	$e + Ar \rightarrow e + e + Ar^+$	Bolsig+	m^3/s	[27], [28], [35]
2	$e + Ar \rightarrow e + Ar(1s)$	Bolsig+	m^3/s	[27], [28]
3	$e + Ar \rightarrow e + Ar(2p)$	Bolsig+	m^3/s	[27], [28]
4	$e + Ar(1s) \rightarrow e + Ar$	Bolsig+	m^3/s	[27], [28]
5	$e + Ar(2p) \rightarrow e + Ar$	Bolsig+	m^3/s	[27], [28]
6	$e + Ar(1s) \rightarrow e + Ar(2p)$	Bolsig+	m^3/s	[36], [37]
7	$e + Ar(2p) \rightarrow e + Ar(1s)$	Bolsig+	m^3/s	[36], [37]
8	$e + Ar(1s) \rightarrow e + e + Ar^+$	Bolsig+	m^3/s	[38]
9	$e + Ar(2p) \rightarrow e + e + Ar^+$	Bolsig+	m^3/s	[38]
10	$e + {Ar_2}^* \rightarrow e + e + {Ar_2}^+$	Bolsig+	m^3/s	[39]
11	$e + {Ar_2}^+ \rightarrow Ar(2p) + Ar$	$1.04x10^{-12}\left({300}/{T_e[\mathrm{K}]}\right)^{0.67}\frac{1-e^{\left(-\frac{418}{T_{vib}[\mathrm{K}]}\right)}}{1-0.31e^{\left(-\frac{418}{T_{vib}[\mathrm{K}]}\right)}}$	m^3/s	[26], [33], [40]
12	$e + {Ar_2}^+ \rightarrow e + Ar^+ + Ar$	$1.11x10^{-12}e^{\left(-\frac{2.94}{T_e[\mathrm{eV}]}+3\frac{T_g[\mathrm{eV}]-0.026}{T_e[\mathrm{eV}]}\right)}$	m^3/s	[33], [40], [41]
13	$e + {Ar_2}^* \rightarrow e + Ar + Ar$	$1.0x10^{-15}$	m^3/s	[42]
14	$Ar(1s) + OH \rightarrow Ar + OH$	$4.0x10^{-16}$	m^3/s	[43], [44]
15	$Ar(1s) + Ar(1s) \rightarrow e + Ar^+ + Ar$	$1.75x10^{-14}(T_g[\mathrm{eV}])^{1/2}$	m^3/s	[33], [40], [45], [46]
16	$Ar(2p) + Ar \rightarrow Ar(1s) + Ar$	$5.0x10^{-18}$	m^3/s	[33], [40], [45], [47]
17	$Ar^+ + Ar + Ar \rightarrow {Ar_2}^+ + Ar$	$2.50x10^{-43}\left({300}/{T_g[\mathrm{K}]}\right)$	m^6/s	[33], [40], [42], [48]
18	$Ar(1s) + Ar + Ar \rightarrow {Ar_2}^* + Ar$	$3.3x10^{-44}$	m^6/s	[33], [40], [42], [45]
19	$Ar(2p) + Ar + Ar \rightarrow {Ar_2}^* + Ar$	$2.5x10^{-44}$	m^6/s	[33], [45], [47]
20	$Ar(2p) \rightarrow Ar(1s)$	$4.4x10^7$	s^{-1}	[40], [49]
21	$Ar(1s) \rightarrow Ar$	$3.1x10^5$	s^{-1}	[40], [49]
22	${Ar_2}^* \rightarrow Ar + Ar$	$6.0x10^7$	s^{-1}	[40], [42]
23	$e \rightarrow e(wall)$	ν_{diff}	s^{-1}	[32]–[34]
24	$Ar^+ \rightarrow Ar^+(wall)$	ν_{diff}	s^{-1}	[32]–[34]
25	${Ar_2}^+ \rightarrow {Ar_2}^+(wall)$	ν_{diff}	s^{-1}	[32]–[34]

where $\mu_o = 1.5x10^{-4}\ \mathrm{m^2V^{-1}s^{-1}}$ is the reduced mobility and P_g is in Torr.

The plasma model is accompanied by an EM model of the photonic crystal and plasma. The EM model was solved by using ANSYS EM19.2, HFSS®. In Fig. 1 the PhC and microplasma configuration is shown. In the upper perspective view, the top of the PhC is removed to reveal the inner structures. The photonic crystal consists of a two-dimensional array of alumina rods ($11x7$) held by a copper frame. MMW power enters and leaves the PhC through two rectangular wave ports in the copper frame. The central rod of the array has been removed to form a vacancy within the crystal where the microplasma is generated. The vacancy acts as a resonator to provide a strong MMW electric field to ignite and sustain the plasma. A detailed description of the PhC configuration can be found in the previous reports [21], [22], [50], [51]. The solution of the EM model will allow the coupling between two models by determining the MMW electric field as a function of electron density as described in the following sections.

2.2 Electromagnetic model

In plasma modeling, there is a self-consistency challenge: the absorbed power depends on the electric field that in turn depends on the electron density. In DC plasmas it is relatively simple to know how much power is dissipated by the plasma (and thus to calculate the electric field) because there is a conduction current that circulates between the electrodes.

Unlike DC plasmas, in this study in the millimeter wave (MMW) range, there are no electrodes nor external conduction currents. There is a complex relationship between the net power P_{net} to the resonant PhC system and the internal electric

field of the plasma. A way to estimate this relationship is through an EM model that uses the Drude equations for the plasma. This simulation method allows one to find the electric field's dependence of the electron density and achieve a simple coupling with the plasma model, by self consistently computing an EM field for every modeled plasma density.

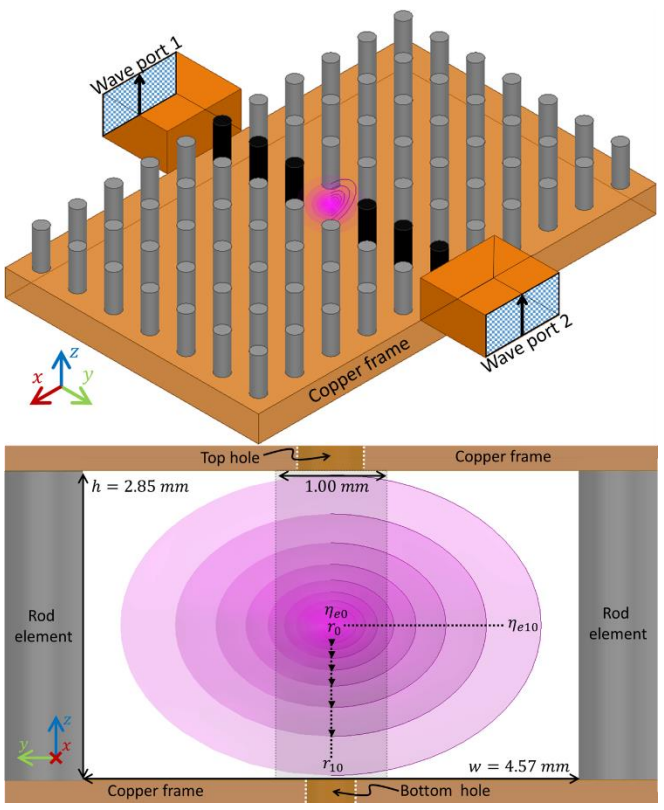

Fig. 1 The photonic crystal geometry and the EM model used for coupling the incident millimeter wave power to the kinetic model.

To model the plasma within the PhC, an electron density gradient has been considered as shown in Fig. 1. This gradient is simplified as a step-wise geometry composed of 10 shells. Each shell is filled with a specified electron density labeled as n_{e1}, n_{e2},… n_{e10} with the respective radius r_1, r_2,… r_{10}, by following the Drude model:

$$\omega_{pe}{}^2 = \frac{e^2 n_e}{m_e \varepsilon_0}, \quad \nu_m \sim 5.7x10^9 P_g \frac{300\ \mathrm{K}}{T_g} \qquad (3)$$

$$\varepsilon_r{}' = 1 - \frac{\left(\omega_{pe}/\omega\right)^2}{1+\left(\nu_m/\omega\right)^2}, \quad \varepsilon_r{}'' = \frac{\left(\omega_{pe}/\omega\right)^2\left(\nu_m/\omega\right)}{1+\left(\nu_m/\omega\right)^2} \qquad (4)$$

where ω and ω_{pe} are the MMW driving frequency and the plasma frequency respectively in rad s^{-1}, m_e is the electron mass in kg, ε_0 is the vacuum permittivity in F/m, ν_m is the collision frequency in s^{-1}, $\varepsilon_r{}'$ and $\varepsilon_r{}''$ are the real and imaginary part of the relative plasma permittivity. Using a simple diffusion model [51] to approximate the electron density distribution, the radially symmetric plasma was modeled by assuming that there is only ionization at the core of the plasma. Then, the radial distribution of the electron density is given by:

$$n_e(r) = n_{e0}\frac{R_{max}}{R_{max}-R_0}\left(\frac{R_0}{r} - \frac{R_0}{R_{max}}\right) \qquad (5)$$

The EM model is pre-solved by calculating the central electric field strength as a function of core electron density: from n_{e0}= 0 (no plasma case) to $n_{e0} = 1.0x10^{20}$ m^{-3} (high power and pressure case). This range is consistent with the magnitude found in the previous reports [21], [51]. In equation (5) R_{max} is the maximum plasma radius obtained from the plasma contours in a previous report [22]. The central plasma core radius is estimated [51] to be $R_0 = 0.07$ mm, and r_n is the radius of every shell in the Drude model given by:

$$r_n = R_0\left(\frac{R_{max}}{R_0}\right)^{0.1n} \qquad (6)$$

Note that for every pressure, the collisional frequency ν_m depends on the pressure itself, but also on the gas temperature at that pressure as described in equation (3). The neutral argon temperatures used in the EM model were taken from measurements in Ref. [22].

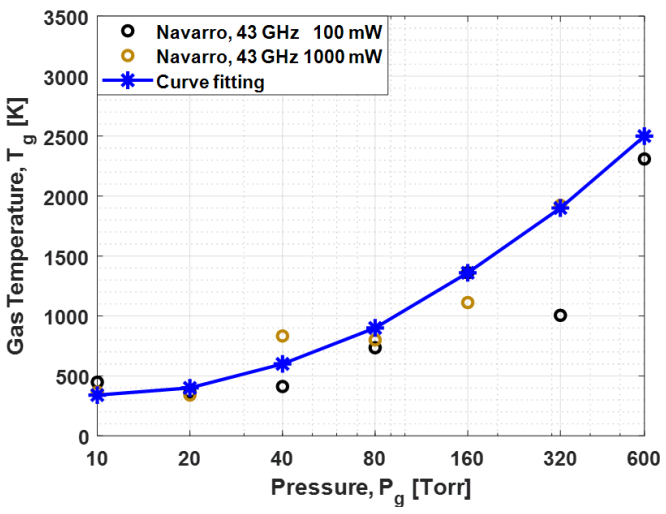

Fig. 2. Curve fitting of argon gas temperature estimated by Lorentzian line shape of the absorption profile at 811.53 nm by using laser diode absorption spectroscopy as a function of the pressure.

This core gas temperature was measured within the central region of the plasma and plotted in Fig. 2. The data are fitted (blue curve), and the result is used in the Drude model, as well as for neutral-neutral and three-body collision rates in the plasma model.

3. Results

3.1 Electric field vs electron density

Fig. 3 shows the core electric field from the EM model as a function of the electron density and pressure of the plasma. For practical purposes, this magnitude was taken as a single-point measurement at the core of the plasma volume. The discrete values of E are represented by the circles in each curve. The computed values of E are fitted by using a 10th-degree polynomial function for each pressure and represented by the solid lines in Fig. 3. These fitted functions are incorporated into the plasma model. As expected, a decrease of the electric field can be observed as the electron density increases due to higher plasma conductivity. Somewhat contrary to intuition, however, as pressure increases the electric field is higher for a constant value of electron density: the plasma having a smaller volume at high pressure, dissipates less power, giving rise to a higher electric field. For the EM model, only two net power levels were solved. For the low (160 mW) and high (1000 mW) net power, the nominal values of the electric field correspond to $E = 0.7x10^5$ Vm^{-1} and $E = 1.75x10^5$ Vm^{-1} respectively.

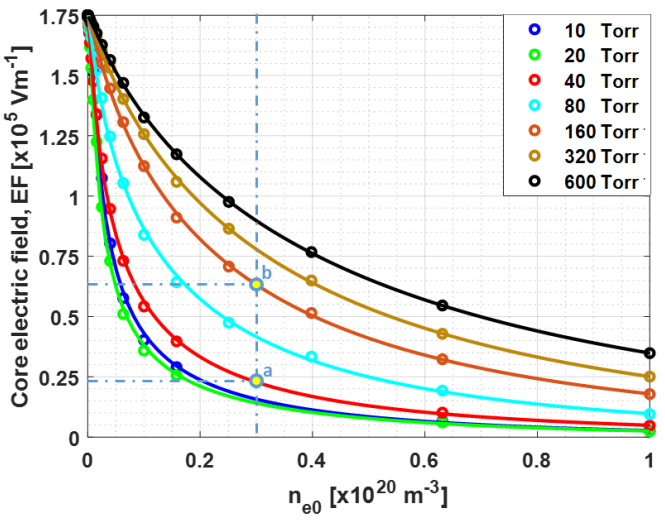

Fig. 3 Electric field at the core of the plasma as a function of the electron density for $P_{net} = 1000$ mW and different gas pressures ($1.3x10^3$ to $8.0x10^4$ Pa). Discrete values from the EM model are shown as circles, and the curve fitting functions are shown as solid lines.

3.2 Self-consistency of the electric field

To demonstrate the self-consistent iteration of the electric field between the plasma model and the EM model, a single pulsed discharge is presented in Fig. 4. At the onset of the EM pulse, the plasma density is low and the electric field is that of the empty PhC ($1.75x10^5$ Vm^{-1}). During the breakdown phase of the plasma, the electron density increases and the modeled electric field decreases due to plasma damping of the PhC, wave reflection, and shielding by free electrons. At approximately 10 μs after the beginning of the pulse, the electron density and internal electric field reach the steady state. At 350 μs the EM pulse ceases ($E = 0$) and the plasma density decays back toward zero.

The pulsed simulations are presented for 40 Torr and 160 Torr. The self-consistent plasma simulations may be compared with the EM simulation of Fig. 3 at $n_e = 3x10^{19}$ m^{-3}, for 40 Torr (point a) and 160 Torr (point b). We note that $E \sim 0.25x10^5$ Vm^{-1} and $E \sim 0.65x10^5$ Vm^{-1} can be observed, respectively, which match with the fields marked (a) and (b) in Fig. 3. This demonstrates that the method for self-consistent calculation of the electric field between ZDPlasKin and HFSS functions well.

3.3 Electron density

In this section the modeled electron density is compared with experimental measurements of the microplasma. We first present the results obtained by assuming a constant gas temperature (300 K). The disagreement between model and experiment, noticeably at higher gas pressures, leads to the development of a two-temperature model. This improved model uses a hot core temperature to model gas rarefaction and a reduction of three-body and neutral-neutral collisions. The two-temperature model assumes a cool outer boundary temperature to accurately predict the slow diffusion loss rates through denser gases at the periphery.

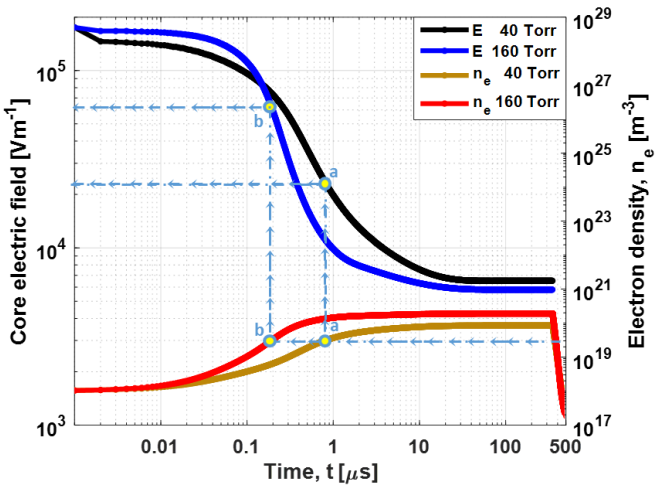

Fig. 4. Evolution in time of the core electric field (black and blue curve) and electron density (yellow and red curve) for a pressure of 40 Torr and 160 Torr ($5.3x10^3$ and $2.1x10^4$ Pa), and $P_{net} = 1000$ mW.

For the constant gas temperature assumption, the modeled electron density is shown in Fig. 5. Note that for the experimental data [21], [51], the electron density increases monotonically with pressure. The modeled density is comparable to the experiment for low pressure, but at higher pressure the simulations predict very low electron density, suggesting a problem in the plasma model.

In order to find the reasons for this inaccurate behavior, the neutral-neutral and three-body collisions in the model reactions were addressed. Recent experimental evidence suggests that the microplasma has a small, hot core during high pressure operation. Gas rarefication in this hot core can dramatically alter neutral collision rates. In Table 1, we note that reactions 11, 12, 15, and 17 are dependent on gas temperature and are related to the loss and production of electrons.

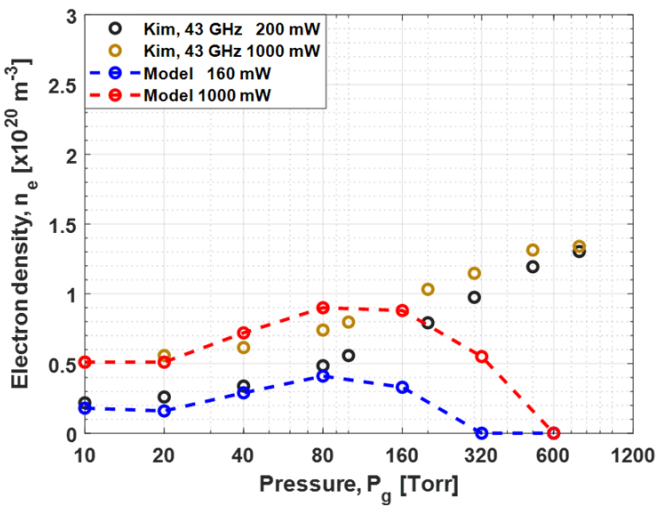

Fig. 5. Preliminary comparison ($T_g = 300$ K) of the electron density from the experimental data [21], [51] (black and yellow circles) and plasma model (blue and red curves) as a function of the pressure.

To improve the performance of the model, we introduce two gas temperatures. The first temperature represents the boundary of the plasma and controls diffusion losses via Eq. (2) to the solid surfaces of the PhC ($T_{g^{diff}} = 300$ K). A second temperature uses data for the experimental gas temperature which was measured at the core of plasma ($T_{g^{core}}$). This core temperature depends on pressure and is found in Fig. 2.

Fig. 6 shows the improved results for the electron density by having taken into account the large spatial variation in gas temperature. In this case, the electron density tends to increase with pressure in agreement with the experimental results. The newly computed electron density at high pressure (above 80 Torr) is much higher and comparable to the experiment. The simulated density at low pressure remains almost the same. This is because at lower pressure (10 Torr and 20 Torr), $T_{g^{core}}$ is close to 300 K , so there was not much influence on the rate constants. Hence, the electron density was not too inaccurate in the simpler one-temperature model.

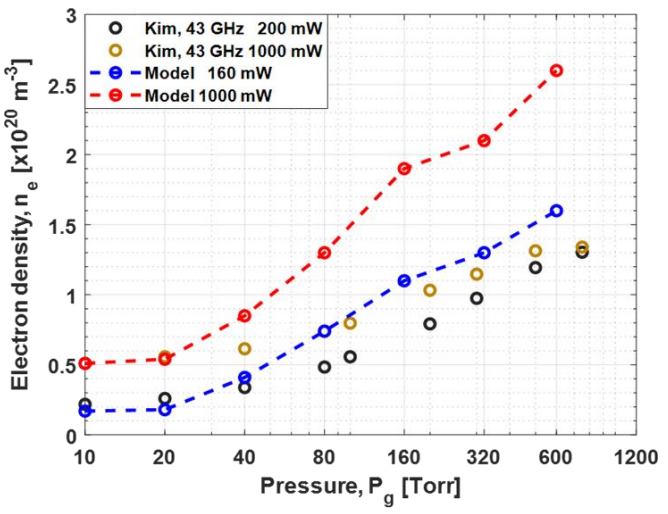

Fig. 6. Comparison of the electron density from experimental data [21], [51] (black and yellow curves) and plasma model (blue and red curves) as a function of the pressure, by including experimental core gas temperatures $T_{g^{core}}$ in the model.

3.4 Metastable density

To further validate the model, Fig. 7 compares the lumped Ar(1s) excited state density with recent measurements using laser diode absorption spectrometry of the Ar($1s_5$) state. The metastable density is observed to decrease for higher pressures in both cases. The loss of metastables is due to electron impact ionization of the excited states, which increases the electron density at higher pressures. The prediction of the model is not perfect, but it produces the correct trend and a reasonable density for a relatively simple model. As was the case for electron density, the two-temperature model was also important in achieving the agreement shown in Fig. 7.

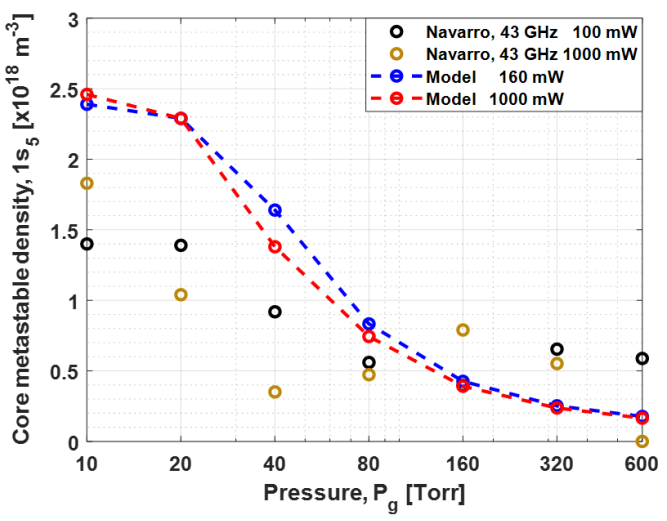

Fig. 7. Comparison of the metastable density for the experimental data [22] (black and yellow curve) and plasma model (blue and red curve) as a function of the pressure, by including $T_{g^{core}}$ in the model.

3.5 Electron temperature

In addition to the electron and metastable density, the electron temperature T_e, reduced electric field E/N_g and the 3-body recombination rate (reaction 17) are shown in Fig.8 for a net power of 1000 mW.

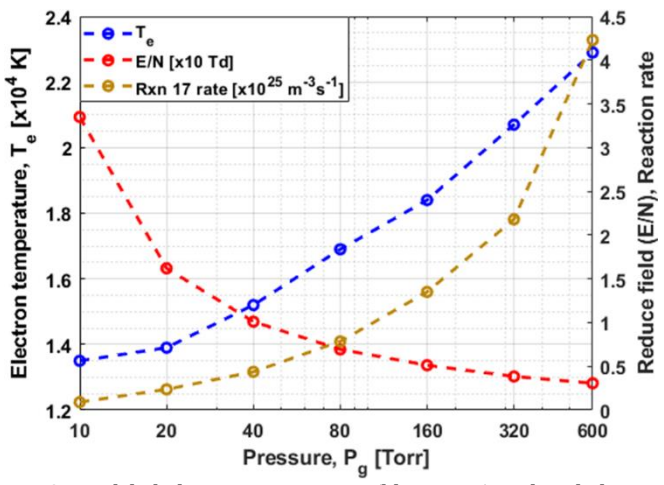

Fig. 8. Modeled electron temperature (blue curve), reduced electric field (red curve) and the 3-body recombination rate (reaction 17 in yellow curve) as a function of the pressure for a $P_{net} = 1000\ mW$.

The electron temperature in the microplasma increases with argon pressure because the losses due to 3-body recombination are increasing. An increase in T_e is needed to enhance the ionization rate to compensate for additional 3-body losses. This loss mechanism forces a higher electon temperature even though there is a decreased reduced electric field inside the plasma.

4. Discussion

Recent experimental measurements show that the argon microplasma consists of a hot, dense core (T_g =~ 2000 K, n_{e0} ~ 10^{20} m^{-3}) that is surrounded by a cool, diffuse plasma. The previous section demonstrates that modeling the microplasma using a simple, uniform gas temperature does not accurately predict the experimentally observed behavior. If the gas temperature is uniformly hot, then diffusion losses are too rapid. On the other hand, if the gas is uniformly cool then neutral-neutral and three-body collisions are too frequent. Both errors result in decreased electron density.

Although this plasma kinetic model is zero-dimensional, we show that reasonable agreement with experiments is possible if (a) diffusion losses to the room-temperature boundaries are assigned a single low temperature (300 K), and (b) those collisions that depend on gas density within the microplasma's core are assigned an elevated temperature. Experimentally, the core temperature is found to be an order of magnitude greater than the boundary region. This temperature gradient causes some collision rates to decrease by one to two orders of magnitude. For example, the loss of the Ar_2^+ ion through recombination collisions (17)→(11)→(5) is suppressed in the hot core, allowing for the observed electron density on the order of 10^{20} m^{-3}.

Previously published models for microplasmas in photonic crystals [12] and for microplasma sustained by MMW and THz radiation [18]–[20] have assumed a single, uniform gas temperature. This simplifying assumption is reasonable at low gas pressures for which three-body processes are unimportant [12]. However, as more sophisticated models are developed, the evidence suggests that modeling both gas heating and temperature diffusion are critical to capturing the correct physics.

5. Conclusion

In this work we have modeled an argon microplasma at 43 GHz using ZDPlaskin and BOLSIG+ plasma kinetics solvers. In order to determine the self-consistent internal electric field from the incident wave power, a separate three-dimensional electromagnetic model was solved using ANSYS HFSS. These two models were associated with each other through a simple coupling, using the EM field vs. electron density function derived from the EM model. Therefore, the internal electric field is found in a consistent manner from modeled plasma density.

Electron density (n_e) and argon metastable density ($1s_5$) were compared with those found experimentally in previous reports. Despite the difficulty of approaching a complex three-dimensional plasma with a zero-dimensional kinetic model, the modeled parameters are in a reasonable agreement with the experiment, but only if the experimental core gas temperature was considered. This observation suggests that microplasma modeling at these frequencies is rather sensitive to the gas temperature at the core of plasma. Accurate first-principles models should carefully consider gas heating and steep temperature gradients.

In future work, we will study the diagnostics and modeling of the pulsed microplasma at 43 GHz as well as at 94 GHz.

Acknowledgments

This work was supported by the U.S. Department of Energy under Award No. DE-SC0021249.

Data availability

The data that supports the findings of this study are available within the article.

References

[1] K. H. Becker, K. H. Schoenbach, and J. G. Eden, "Microplasmas and applications," *J. Phys. D: Appl. Phys.*, vol. 39, no. 3, pp. R55–R70, Jan. 2006, doi: 10.1088/0022-3727/39/3/R01.

[2] M. Miclea, K. Kunze, G. Musa, J. Franzke, and K. Niemax, "The dielectric barrier discharge — a powerful microchip plasma for diode laser spectrometry," *Spectrochimica Acta Part B: Atomic Spectroscopy*, vol. 56, no. 1, pp. 37–43, Jan. 2001, doi: 10.1016/S0584-8547(00)00286-X.

[3] K. Kunze, M. Miclea, G. Musa, J. Franzke, C. Vadla, and K. Niemax, "Diode laser-aided diagnostics of a low-pressure dielectric barrier discharge applied in element-selective detection of molecular species," *Spectrochimica Acta Part B: Atomic Spectroscopy*, vol. 57, no. 1, pp. 137–146, Jan. 2002, doi: 10.1016/S0584-8547(01)00359-7.

[4] I. E. Kieft, E. P. v d Laan, and E. Stoffels, "Electrical and optical characterization of the plasma needle," *New J. Phys.*, vol. 6, pp. 149–149, Oct. 2004, doi: 10.1088/1367-2630/6/1/149.

[5] B. Niermann, M. Böke, N. Sadeghi, and J. Winter, "Space resolved density measurements of argon and helium metastable atoms in radio-frequency generated He-Ar micro-plasmas," *Eur. Phys. J. D*, vol. 60, no. 3, pp. 489–495, Dec. 2010, doi: 10.1140/epjd/e2010-00166-8.

[6] A. M. Bilgic, U. Engel, E. Voges, M. Kückelheim, and J. A. C. Broekaert, "A new low-power microwave plasma source using microstrip technology for atomic emission spectrometry," *Plasma Sources Sci. Technol.*, vol. 9, no. 1, pp. 1–4, Jan. 2000, doi: 10.1088/0963-0252/9/1/301.

[7] J. Kim and K. Terashima, "2.45 GHz microwave-excited atmospheric pressure air microplasmas based on microstrip technology," *Appl. Phys. Lett.*, vol. 86, no. 19, p. 191504, May 2005, doi: 10.1063/1.1926411.

[8] Y. Hidaka, E. M. Choi, I. Mastovsky, M. A. Shapiro, J. R. Sirigiri, and R. J. Temkin, "Observation of Large Arrays of Plasma Filaments in Air Breakdown by 1.5-MW 110-GHz Gyrotron Pulses," *Phys. Rev. Lett.*, vol. 100, no. 3, p. 035003, Jan. 2008, doi: 10.1103/PhysRevLett.100.035003.

[9] J. Xue and J. A. Hopwood, "Microwave-Frequency Effects on Microplasma," *IEEE Transactions on Plasma Science*, vol. 37, no. 6, pp. 816–822, Jun. 2009, doi: 10.1109/TPS.2009.2015453.

[10] H. Kim and J. Hopwood, "Plasma-enhanced metamaterials using microwave radiative power transfer," *Plasma Sources Science and Technology*, vol. 27, no. 9, Art. no. 9, Sep. 2018, doi: 10.1088/1361-6595/aadb64.

[11] P. K. Singh, J. Hopwood, and S. Sonkusale, "Metamaterials for Remote Generation of Spatially Controllable Two Dimensional Array of Microplasma," *Sci Rep*, vol. 4, no. 1, p. 5964, May 2015, doi: 10.1038/srep05964.

[12] J. Gregório, S. Parsons, and J. Hopwood, "Reconfigurable photonic crystal using self-initiated gas breakdown," *Plasma Sources Sci. Technol.*, vol. 26, no. 2, p. 02LT03, Jan. 2017, doi: 10.1088/1361-6595/26/2/02LT03.

[13] S. Parsons, J. Gregório, and J. Hopwood, "Microwave plasma formation within a 2D photonic crystal," *Plasma Sources Sci. Technol.*, vol. 26, no. 5, p. 055002, Mar. 2017, doi: 10.1088/1361-6595/aa62ed.

[14] I. Adamovich *et al.*, "Plasma: at the frontier of scientific discovery," USDOE Office of Science (SC) (United States), Apr. 2017. doi: 10.2172/1615243.

[15] T. W. Crowe, W. L. Bishop, D. W. Porterfield, J. L. Hesler, and R. M. Weikle, "Opening the terahertz window with integrated diode circuits," *IEEE Journal of Solid-State Circuits*, vol. 40, no. 10, pp. 2104–2110, Oct. 2005, doi: 10.1109/JSSC.2005.854599.

[16] S. G. Parsons and J. Hopwood, "Millimeter Wave Plasma Formation Within a 2D Photonic Crystal," *IEEE Electron Device Lett.*, vol. 38, no. 11, pp. 1602–1605, Nov. 2017, doi: 10.1109/LED.2017.2750486.

[17] J. Hopwood, "94 GHz microplasma sustained by a photonic crystal," *Plasma Sources Sci. Technol.*, vol. 30, no. 11, p. 115013, Nov. 2021, doi: 10.1088/1361-6595/ac3213.

[18] J. Gregório, A. R. Hoskinson, and J. Hopwood, "Modeling of microplasmas from GHz to THz," *Journal of Applied Physics*, vol. 118, no. 8, p. 083305, Aug. 2015, doi: 10.1063/1.4928468.

[19] A. Alamatsaz and A. Venkattraman, "A kinetic study of electron heating and plasma dynamics in microwave microplasmas," *Physics of Plasmas*, vol. 26, no. 1, p. 013512, Jan. 2019, doi: 10.1063/1.5082307.

[20] D. Levko and L. L. Raja, "Microwave microplasma parameters at extremely high driving frequencies," *Physics of Plasmas*, vol. 26, no. 1, p. 014505, Jan. 2019, doi: 10.1063/1.5058065.

[21] H. Kim, S. Parsons, and J. Hopwood, "Spectroscopic diagnostics of continuous and transient microplasma formed in a millimeter wave photonic crystal," *Plasma Sources Sci. Technol.*, vol. 29, no. 4, p. 045001, Mar. 2020, doi: 10.1088/1361-6595/ab75a0.

[22] R. Navarro and J. Hopwood, "Argon metastable density and temperature of a 43 GHz microplasma," *Journal of Applied Physics*, vol. 131, no. 1, p. 013305, Jan. 2022, doi: 10.1063/5.0065505.

[23] S. Pancheshnyi, B. Eismann, G. J. M. Hagelaar, and L. C. Pitchford, "Computer code ZDPlasKin." http://www.zdplaskin.laplace.univ-tlse.fr (University of Toulouse, LAPLACE, CNRS-UPS-INP, Toulouse, France, 2008)

[24] G. J. M. Hagelaar and L. C. Pitchford, "Solving the Boltzmann equation to obtain electron transport coefficients and rate coefficients for fluid models," *Plasma Sources Sci. Technol.*, vol. 14, no. 4, pp. 722–733, Oct. 2005, doi: 10.1088/0963-0252/14/4/011.

[25] N. Miura, J. Xue, and J. A. Hopwood, "Argon Microplasma Diagnostics by Diode Laser Absorption," *IEEE Trans. Plasma Sci.*, vol. 38, no. 9, pp. 2458–2464, Sep. 2010, doi: 10.1109/TPS.2010.2053854.

[26] A. J. Cunningham, T. F. O'Malley, and R. M. Hobson, "On the role of vibrational excitation in dissociative recombination," *J. Phys. B: At. Mol. Phys.*, vol. 14, no. 4, pp. 773–782, Feb. 1981, doi: 10.1088/0022-3700/14/4/024.

[27] Á. Yanguas-Gil, J. Cotrino, and L. L. Alves, "An update of argon inelastic cross sections for plasma discharges," *J. Phys. D: Appl. Phys.*, vol. 38, no. 10, pp. 1588–1598, May 2005, doi: 10.1088/0022-3727/38/10/014.

[28] L. L. Alves, "The IST-LISBON database on LXCat," *J. Phys.: Conf. Ser.*, vol. 565, p. 012007, Dec. 2014, doi: 10.1088/1742-6596/565/1/012007.

[29] E. Carbone *et al.*, "Data Needs for Modeling Low-Temperature Non-Equilibrium Plasmas: The LXCat Project, History, Perspectives and a Tutorial," *Atoms*, vol. 9, no. 1, p. 16, Feb. 2021, doi: 10.3390/atoms9010016.

[30] L. C. Pitchford *et al.*, "LXCat: an Open-Access, Web-Based Platform for Data Needed for Modeling Low Temperature Plasmas," *Plasma Processes and Polymers*, vol. 14, no. 1–2, p. 1600098, 2017, doi: 10.1002/ppap.201600098.

[31] S. Pancheshnyi *et al.*, "The LXCat project: Electron scattering cross sections and swarm parameters for low temperature plasma modeling," *Chemical Physics*, vol. 398, pp. 148–153, Apr. 2012, doi: 10.1016/j.chemphys.2011.04.020.

[32] E. Basurto, J. de Urquijo, I. Alvarez, and C. Cisneros, "Mobility of He^{+}, Ne^{+}, Ar^{+}, N_{2}^{+}, O_{2}^{+}, and CO_{2}^{+} in their parent gas," *Phys. Rev. E*, vol. 61, no. 3, pp. 3053–3057, Mar. 2000, doi: 10.1103/PhysRevE.61.3053.

[33] A. R. Hoskinson, J. Gregorío, J. Hopwood, K. Galbally-Kinney, S. J. Davis, and W. T. Rawlins, "Argon metastable production in argon-helium microplasmas," *Journal of Applied Physics*, vol. 119, no. 23, p. 233301, Jun. 2016, doi: 10.1063/1.4954077.

[34] W. Lindinger, "Mobilities of various mass-identified positive ions in helium and argon," *J. Chem. Phys.*, vol. 62, no. 9, p. 3517, 1975, doi: 10.1063/1.430988.

[35] L. C. Pitchford *et al.*, "Comparisons of sets of electron–neutral scattering cross sections and swarm parameters in noble gases: I. Argon," *J. Phys. D: Appl. Phys.*, vol. 46, no. 33, p. 334001, Aug. 2013, doi: 10.1088/0022-3727/46/33/334001.

[36] J. Bretagne, G. Delouya, and J. Godart, "High-energy electron distribution in an electron-beam-generated argon plasma," p. 16.

[37] J. Bretagne, J. Godart, and V. Puech, "Low-energy electron distribution in an electron-beam-generated argon plasma," *J. Phys. D: Appl. Phys.*, vol. 15, no. 11, pp. 2205–2225, Nov. 1982, doi: 10.1088/0022-3727/15/11/014.

[38] L. Vriens, "Physical Laboratory of the University, Utrecht, Netherlands," *PHYSICS LETTERS*, vol. 8, no. 4, p. 2.

[39] K. J. McCann, M. R. Flannery, and A. Hazi, "Theoretical cross sections for ionization of metastable excimers Ne* $_2$ and Ar* $_2$ by electron impact," *Appl. Phys. Lett.*, vol. 34, no. 9, pp. 543–545, May 1979, doi: 10.1063/1.90880.

[40] J. Gregório, P. Leprince, C. Boisse-Laporte, and L. L. Alves, "Self-consistent modelling of atmospheric micro-plasmas produced by a microwave source," *Plasma Sources Sci. Technol.*, vol. 21, no. 1, p. 015013, Feb. 2012, doi: 10.1088/0963-0252/21/1/015013.

[41] J. Jonkers, M. van de Sande, A. Sola, A. Gamero, A. Rodero, and J. van der Mullen, "The role of molecular rare gas ions in plasmas operated at atmospheric pressure," *Plasma Sources Sci. Technol.*, vol. 12, no. 3, pp. 464–474, Jul. 2003, doi: 10.1088/0963-0252/12/3/323.

[42] F. Kannari, A. Suda, M. Obara, and T. Fujioka, "Theoretical simulation of electron-beam-excited xenon-chloride (XeCl) lasers," *IEEE Journal of Quantum Electronics*, vol. 19, no. 10, pp. 1587–1600, Oct. 1983, doi: 10.1109/JQE.1983.1071763.

[43] W. T. Rawlins, K. L. Galbally-Kinney, S. J. Davis, A. R. Hoskinson, and J. A. Hopwood, "Laser excitation dynamics of argon metastables generated in atmospheric pressure flows by microwave frequency microplasma arrays," San Francisco, California, United States, Mar. 2016, p. 97290B. doi: 10.1117/12.2212888.

[44] I. Stefanović, T. Kuschel, S. Schröter, and M. Böke, "Argon metastable dynamics and lifetimes in a direct current microdischarge," *Journal of Applied Physics*, vol. 116, no. 11, p. 113302, Sep. 2014, doi: 10.1063/1.4895714.

[45] A. R. Hoskinson, J. Gregório, S. Parsons, and J. Hopwood, "Electron confinement and heating in microwave-sustained argon microplasmas," *Journal of Applied Physics*, vol. 117, no. 16, p. 163301, Apr. 2015, doi: 10.1063/1.4919416.

[46] V. Puech, "An examination of energy transfers and kinetic mechanisms in argon and in an argon-hydrogen medium excited by an electron beam Application in research on new lasers," 1981. Accessed: Apr. 01, 2022. [Online]. Available: https://ui.adsabs.harvard.edu/abs/1981PhDT.....28P

[47] S. K. Lam, C.-E. Zheng, D. Lo, A. Dem'yanov, and A. P. Napartovich, "Kinetics of Ar $^*_2$ in high-pressure pure argon," *J. Phys. D: Appl. Phys.*, vol. 33, no. 3, pp. 242–251, Feb. 2000, doi: 10.1088/0022-3727/33/3/310.

[48] D. C. Lorents, "The physics of electron beam excited rare gases at high densities," *Physica B+C*, vol. 82, no. 1, pp. 19–26, Mar. 1976, doi: 10.1016/0378-4363(76)90265-5.

[49] A. Kramida, Yu. Ralchenko, J. Reader, and NIST ASD Team(2021), "NIST Atomic Spectra Database (version 5.9), [Online]. Available: https://physics.nist.gov/asd [Thu Mar 31 2022]. National Institute of Standards and Technology, Gaithersburg, MD. DOI:https://doi.org/10.18434/T4W30F".

[50] H. Kim and J. Hopwood, "Tunable millimeter wave photonic crystal for limiting high power pulses using weakly ionized steady state plasma," *Journal of Applied Physics*, vol. 128, no. 9, p. 093302, Sep. 2020, doi: 10.1063/5.0018252.

[51] H. Kim and J. Hopwood, "*In situ* millimeter wave spectroscopy of microplasma within a photonic crystal," *Journal of Applied Physics*, vol. 129, no. 3, p. 033301, Jan. 2021, doi: 10.1063/5.0032522.